Vital Signs Monitoring Using a 26 GHz OFDM Multibeam Testbed

Miquel Sellés Valls
University of Twente (EEMCS)
Enschede, The Netherlands
m.sellesivalls@student.utwente.nl

dr. Yang Miao (Daily Supervisor)
dr. ir. A. B. J. Kokkeler (Committee Chair)
dr. Ying Wang (Committee Member)
University of Twente (EEMCS)
Enschede, The Netherlands
{y.miao a.b.j.kokkeler,ying.wang}@utwente.nl

prof. Sofie Pollin (Committee Member)
KU Leuven (ESAT)
Leuven, Belgium
sofie.pollin@kuleuven.be

***Abstract*—This paper presents a novel pipeline for vital sign monitoring using a 26 GHz OFDM multi-beam testbed. In the context of Joint Communication and Sensing (JCAS), the advanced communication capability at millimeter-wave bands is comparable to the radio resource of radars and hence is able to sense the surrounding environment while communicating. The proposed processing pipeline leverages 20 MHz and 16 spatially orthogonal beams with 7° Half Power Beam Width (HPBW) to estimate vital sign activity in single and multi-person static scenarios directly from raw Channel State Information (CSI) samples. The proposed pipeline employing phase time-frequency calibration methods and Discrete Wavelet Transform (DWT) to improve the performance of conventional Fast Fourier Transform (FFT) based methods in single person scenario is described in detail. A frequency-domain comparison between single and multi-person scenarios is also studied and a $k-$means clustering algorithm introduced to extract breath and heartbeat frequency rates from static persons. According to experimental results, individual transmit (Tx) and receive (Rx) pair links can achieve below 2 bpm error in static single-person monostatic configuration when compared directly to the ground-truth, for both breath and heartbeat activity using the proposed DWT method for a human seating in front and up to 2 m from the Tx/Rx. In static multi-person configuration, individual Tx and Rx pair links achieve less than 2 bpm estimation error in a JCAS scenario employing the proposed joint FFT and k-means method, when two humans are seating at distances below 4 m from the Rx. The presented research work is a promising first step in vital signs monitoring using an active mmWave multibeam communication system, which is promising for practical JCAS applications.**

***Index Terms*—Joint communication and sensing, vital signs monitoring, mmWave multibeam communication**

I. Introduction

As current mobile communication networks mature, it has been well-established that the new era of mobile radio technologies will be far beyond communications alone. It is envisioned that the future mobile communication generation, 6G, will offer truly intelligent wireless systems that will provide both ubiquitous communication and high accuracy localization and high-resolution sensing services [1]. With the objective to integrate communication and sensing functions, Joint Communication and Sensing (JCAS) emerges as a decisive research topic to improve Spectral Efficiency (SE) and support novel applications such as autonomous driving and remote health monitoring.

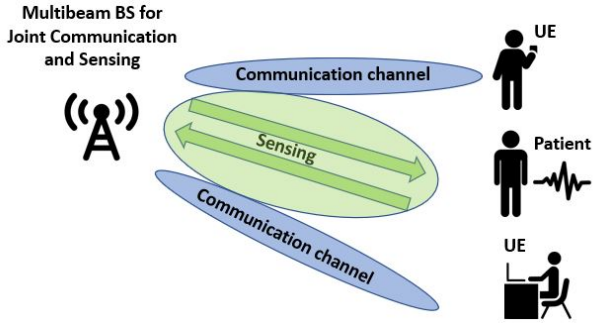

Fig. 1: Considered JCAS system model with multibeam BS, adopting joint waveform for sensing and communication activities.

In this context, multibeam millimeter-wave (mmWave) radio systems can provide simultaneous high-speed communication and accurate sensing at the same frequency band [2]–[4]. Utilizing the orthogonal frequency-division multiplexing (OFDM) signal waveform at the multi-beam base station (BS), the transmit signal can be reflected back (back scattering) from real-world targets and received back at the BS for sensing, or can be propagated through the media and arrive at the user equipment (UE) for communicating. A sketch of this scenario can be seen in Fig. 1. Thanks to the frequency diversity provided by OFDM transmissions, the total number of OFDM symbols in the whole waveform can be split into a number of subcarriers dedicated to active communication, and the remainder of them for simultaneous sensing [5].

Alongside contact-free localization and tracking, the ability to measure and monitor vital signs in real time in a contact-free manner, is a very interesting sensing application in the current healthcare sector. Such capability can help to a great extent with disease early diagnosis and prevention [6], [7]. Vital signs monitoring systems can take the form of either intrusive or contact-free non-intrusive solutions [8]. Among them, intrusive techniques are usually cumbersome and not comfortable for

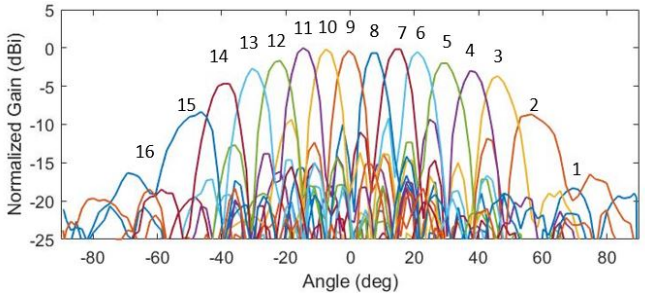

Fig. 2: Beam pattern of the Butler matrix at 26 GHz

long-term monitoring; moreover, it requires the target him-/herself to initiate the monitoring process, which might lead to a reduced usage or the risk for delayed action. Therefore, contact-free RF-based vital signs monitoring constitutes a good solution to avoid interference with the patient's daily activities and can operate continuously [9]. To match the performance of the intrusive monitoring systems, the contact-free solutions need to differentiate vital sign information from different patients, as well as to relate the measured signals to their associated targets. Specific radar systems and communication systems with specific antenna array topology (normally redundant for communication purpose, e.g., multiple distributed Wi-Fi modules) provide high-accuracy localization and real time vital sign estimation in single and multi-person scenarios [10]. Nevertheless, neither of these investigations are conducted with active mmWave communication devices, which limits the current vision of the performance of these systems in actual communication scenarios. In lieu of costly sensing systems, which require complex and specific design solutions, integrated multibeam mmWave JCAS gives birth to an ideal solution to this problem by utilizing active communication systems to seamlessly provide both enhanced performance to the network and spatial monitoring capabilities. Hence, the proposed solution enables an early method for combining active communication activities and monitoring the vital signs of patients in indoor scenarios suitable for healthcare applications.

The remainder of this paper is organized as follows. Section II gives an overview of the state-of-the-art of the vital sign monitoring using communication devices and further elaborates the contributions of the paper. Section IV explains the proposed pipeline and methodology for vital sign estimation for single and multi-person scenarios. Section III introduces the measurement campaign. In Section V, numerical analyses based on real-world measurement are performed and the performance of the proposed pipeline is evaluated. Finally, conclusions and future lines of work are drawn in section VI.

II. Related Work

The examined literature includes a wide variety of approaches tailored towards specific needs and applications. Vital signs contact-free monitoring solutions based on radio signals can be grouped depending on their working frequency band. In sub-6 GHz, research efforts mainly focus on studying the ability of commodity wireless communication systems for breathing and heartbeat estimation in single and multi-person scenario. Additionally, there are existing efforts studying the use of specific wideband RF systems, such as ultra-wide band (UWB), in the sub-6 GHz range exploiting large bandwidths to leverage a better delay/range resolution. At mmWave frequencies, most of the work concentrates on exploiting radar sensing systems for vital sign monitoring. One example of civilian-use mmWave radar is the frequency modulated continuous wave (FMCW) multiple-input and multiple-output (MIMO) radar at 77 GHz [11], initially intended for automotive applications and rising up to be one of the most attractive solutions due to their inherent sensing capabilities provided by the waveform and a large bandwidth.

A. Sub-6 GHz Vital Sign Monitoring

Early approaches of RF-based vital sign estimation can be found in the works of [12], [13] and [14]. These first efforts mainly focused on captured received signal strength (RSS) and phase channel state information (CSI) acquired from WiFi commodity systems to obtain breathing information in single person scenario. Although being a very important step into contactless vital sign monitoring, the aforementioned efforts present some practical limitations. Due to the omni-directional nature of 2.4/5 GHz WiFi signals and the resulting multi-scattering between multiple targets, it becomes difficult to separate the vital signs of different targets with the same breathing rates. Another limitation is that heartbeat estimation is not possible, because the small scale movement of the chest directly linked to heartbeat movement cannot be captured as it is largely camouflaged by the larger displacement due to breathing activity. The WiFi signal can be reflected from many indoor objects in multi-path rich indoor environments, making the recovery of the human reflected signal difficult. Further research efforts employing WiFi signals for vital signs estimation can be found in the works of [15] and [16]. In [15], the authors propose PhaseBeat, a method to exploit CSI phase difference data between two antennas at the receiver end, based on a rigorous analysis with respect to its stability and periodicity. They first calibrate the CSI difference data by removing direct current (dc) and high frequency noises. After downsampling the cleaned data, they select the subcarrier with larger variance for breath and heart rate estimation. To tackle the multi-person scenario, a Root-MUSIC method is used to distinguish the different frequency tones, whereas for the single-person scenario, a FFT-based peak search is performed to extract the estimated rates. They obtain estimation accuracy above 95% for breath and heart rates for the single-person scenario, and 95%, 90% and 80% accuracy for 2, 3 and 4 person scenario, with respect to ground-truth breath and heart rates obtained with a NEULOG Respiration Monitor and a fingertip pulse oximeter, respectively. Moreover, they show that estimation performance degrades as the distance between the transmitter and receiver increases. At 1 m, they obtain 0.15 bpm mean estimation error, whereas at 5 m this increases to

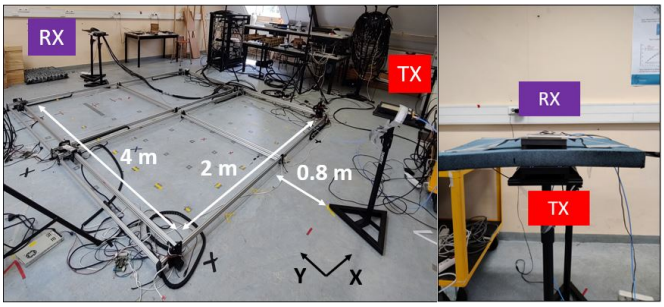

Fig. 3: Testing area. Communication (left) and monostatic Tx/Rx configuration (right)

0.2 bpm, and at 11 m is above 0.4 beats per minute (bpm). In [16], a joint angle of arrival - time of flight (AoA-ToF) beamformer is proposed at each packet time. To deal with the small ToF resolution that the 40 MHz commodity WiFi yields, a Singular Value Decomposition (SVD) algorithm is utilized to reformulate the problem with reduced dimensions by decomposing the data matrix into the signal and noise subspaces. The estimated AoA-ToF grid after SVD is then multiplied by the time domain symbol signal, which yields a time domain signal representing the phase variations due to chest displacement. Single-person scenario results in line-of-sight (LoS) and non-light-of-sight (NLoS) condition and up to a distance of 4 m between transmitter and receiver yield $> 99\%$ median accuracy with respect to the ground-truth. In [17], *Eid et al.* propose HoloTag, an ultralow-cost ultra high frequency (UHF) radio-frequency identification (RFID) array-based system over which a holographic projection of its environment is measured and utilized to localize and monitor the vital signs of several targets. Using minimum variance distortionless response (MVDR) beamforming for AoA estimation and a FFT-based vital sign estimation method, the proposed system achieves 11° and 17° AoA median error, for single and two-person scenario, respectively. Breathing rate estimation error is kept under 0.4 bpm and 0.5 bpm for more than 60% of trials for single and two-person scenario, respectively. *Zhang et al.* present MTrack [18] a 2 GHz wideband system that generates signals between 4-6 GHz. Equipped with one transmitter antenna and 16 receiver antennas, the system relies on AoA-ToF beamforming with a path selection algorithm to suppress interference from dynamic multipaths in order to detect and track individual signals under multiperson conditions. The proposed system is capable of localizing and tracking people's trajectories with a 20 cm error at a maximum distance of 7 m for both LoS and NLoS scenarios. Vital sign estimation achieves $>99\%$ median accuracy for both breath and heartbeat rates. *Chenglong et al.* establish in [19] a sub-6 GHz radar-like MIMO-OFDM prototype for contact-free localization and human tracking in real-time. The pedestrian is localized directly from CSI samples using a particle filter-based hologram tracking algorithm. Experimental evaluation shows that the proposed algorithm can achieve about 20 cm mean tracking accuracy in real-time.

TABLE I
mMWave Multibeam Testbed Parameters Setting

System parameter	Value
Transmit power	15 dBm
Tx/Rx Gain	31 dB
Center frequency	26 GHz
Bandwidth	20 MHz
Subcarrier spacing	15 kHz
# Subcarriers	100
Modulation	16-QAM
Sampling rate	200 Hz

B. mmWave Vital Sign Monitoring

In the mmWave frequencies, research efforts are mainly focused on the use of radar(-like) systems. In [20], a 8 GHz FMCW radar is used alongside a multi-person tracking algorithm to localize targets and extract their time domain phase difference data for estimating chest displacements due to breathing and heartbeat activities. From the presented experiments, the algorithm is capable of keeping the error below 3 bpm during 90% of the measured time. Similarly, authors in [21] and [22] use a 77 GHz FMCW MIMO radar to localize humans in range and angular domain before extracting their time domain phase difference data. Evaluations under a two-person scenario show that the system is capable of achieving error of less than 1 bpm breath rate, and 3 bpm heart rate at a target-to-radar distance of 1.6 m, with a minimal 40° angular separation between targets. Research efforts have also been made towards the 60 GHz band of the mmWave spectrum. In [23], the authors present a study on the use of maximum ratio combining (MRC) on a UWB 2×4 MIMO radar to improve the signal-to-noise ratio (SNR). This technique leads to a 18% improvement in heart rate estimation accuracy with respect to estimation obtained directly from each Tx-Rx branch. Lastly, a 24 GHz FMCW radar is used in [24] to propose a method for processing the captured time domain phase signal to estimate breath and heart rates in single-person scenario. This includes detrending the original signal and performing continuous wavelet transform (CWT) to obtain a fine tuning of the frequency subspaces. CWT is also used in [20] to separate breath and heart rate frequencies.

C. Contributions of This Paper

As discussed above, from early stages researches have leveraged sub-6 GHz commodity WiFi systems to propose a low-cost, low-complexity solution for contact-free RF-based vital signs monitoring which performs well in single-person and in multi-person scenarios when the breathing and heart rates are sufficiently different. To overcome such limitations, specific solutions are proposed in the literature such as UHF tags [17] or UWB systems [18]. With the unlocking of the 26 GHz and 77 GHz band for the automotive industry, efforts have been concentrated in the use of radar systems for vital sign estimation. Mostly based on FMCW and equipped with MIMO capabilities, these systems are very suitable for vital sign monitoring, as their large bandwidth and multiple antennas

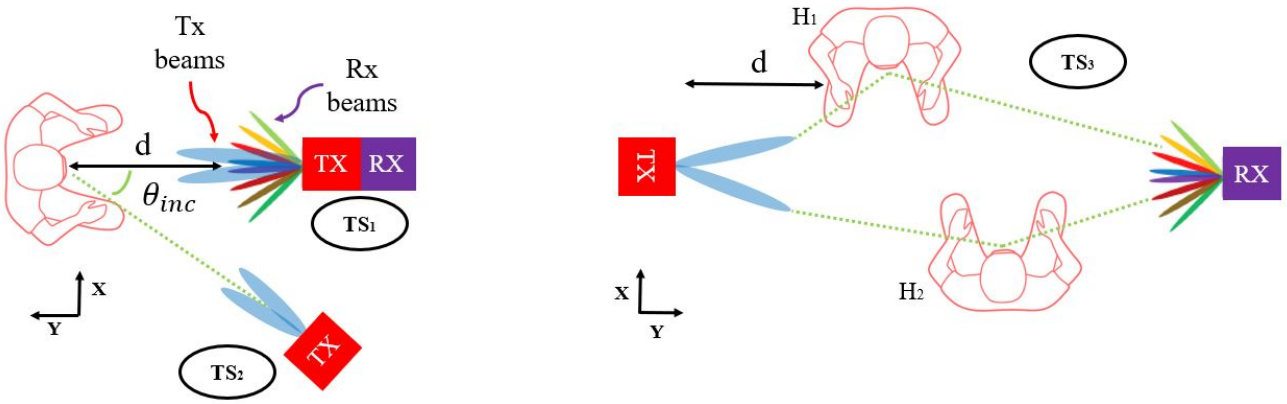

Fig. 4: Testing scenarios. TS_1: single-person adopting monostatic configuration. TS_2: single-person multistatic configuration is used to study the influence of incidence angle on estimation performance. TS_3: downlink JCAS configuration. Tx acting as BS and RX as UE to study the sensing capabilities on two-person scenario.

allow them to localize multiple targets and makes them very sensitive to small-scale chest displacements produced by the breath and heartbeat movements.

To the best of our knowledge, none of the reviewed vital sign monitoring research efforts contemplate the possibility of joint communication and sensing in the framework of active mmWave multibeam communication systems. The contribution of this research work serves as first study of the raw vital sign sensing capabilities of mmWave multibeam communication. The work includes the design and implementation of a processing pipeline to obtain vital sign information from single and multi-person scenarios directly from CSI samples in multibeam mmWave communication. The work introduced in this paper exploits spatial diversity in multibeam transmission along frequency diversity provided by the OFDM subcarriers to obtain accurate vital sign information in single and multi-person indoor scenarios.

III. Experiment and System Overview

A. Prototype and Experiment

The mmWave MIMO testbed from the KU Leuven ESAT department consists of a pair of Butler matrix units, a mmWave front-end operating in the 26 GHz band and multiple Universal Software Radio Peripheral (USRPs). The Butler matrix used in this testbed is the one thoroughly depicted in [25]. The system is able to either transmit or receive up to 16 frequency dependant spatially-orthogonal beams. The beam pattern of the Butler matrix at 26 GHz is shown in Fig. 2. It is noticeable how the center beams have narrower beamwidth and higher gain, up to 20 dB, compared to those at the edge. The USRP transmitting intermediate frequency f_{IF} of 2.4 GHz with 20 MHz bandwidth is used to generate the f_{RF} mmWave signal in the transmitter end. The IF signal serves as input to the Butler matrix, and the ERASynth+ RF signal generator with operating frequency of $f_{LO} = 11.8$ GHz is connected to the local oscillator port of the Butler matrix [26]. The RF up/downconversion in a Butler matrix follows the relation of $f_{RF} = 2f_{LO} + f_{IF}$ [27]. In the receiver end of the Butler matrix, all 16 beams are used to receive signals from different directions from all transmitting beams. Therefore, all available ports of the Rx Butler matrix are employed and connected to the 16 input ports of the receiver USRPs, while the local oscillator port of the Butler matrix is connected to the signal generator, which is synchronized for both Tx and Rx Butler matrices using Pulse Per Second (PPS) and 10 MHz clock reference signals. All USRPs run LabView Communications MIMO Application Framework [28] with a Time Division Duplexing (TDD) signal frame structure with OFDM symbols.

The testing area is shown in Fig. 3 and is a 2×4 m^2 measurement space in a lab room of the department of electrical engineering at the KU Leuven. Three testing scenarios (TS) have been performed to obtain measurement data conveying different perspectives. Due to hardware limitation, only the 2 central beams (beam 8 and 9) of the 16 available ports on the Tx Butler matrix are employed. On the Rx end, all 16 beams are used. The communication system transmit power P_T is set to 15 dBm and 31 dB gain is introduced in both Tx and Rx ends. An uplink (UL) pilot tone is used to estimate the channel using 100 OFDM subcarriers with 15 kHz subcarrier spacing and a channel bandwidth of 20 MHz. The symbol duration is set to 66.67 μs with a cyclic prefix duration of 5.21 μs. We transmit 1 UL pilot symbol per subframe slot. Such slot has a duration of 0.5 ms. In all experiments, 5 s of data are captured, corresponding to a total of 10000 symbols. The complete radio frame format used in the testbed can be found in [29]. The modulation scheme used is 16-QAM. The system parameters setting are summarized in Table I.

To capture the ground-truth vital signs values, we use the available TMSi Mobi device from the biomedical signals and systems group of the electrical engineering department at the University of Twente. Device specification documents can be found in [30]. Using two ports from the device, we obtain the heartbeat rate via a pulse oximeter fingertip sensor and the breathing rate via a respiratory monitor belt around the chest

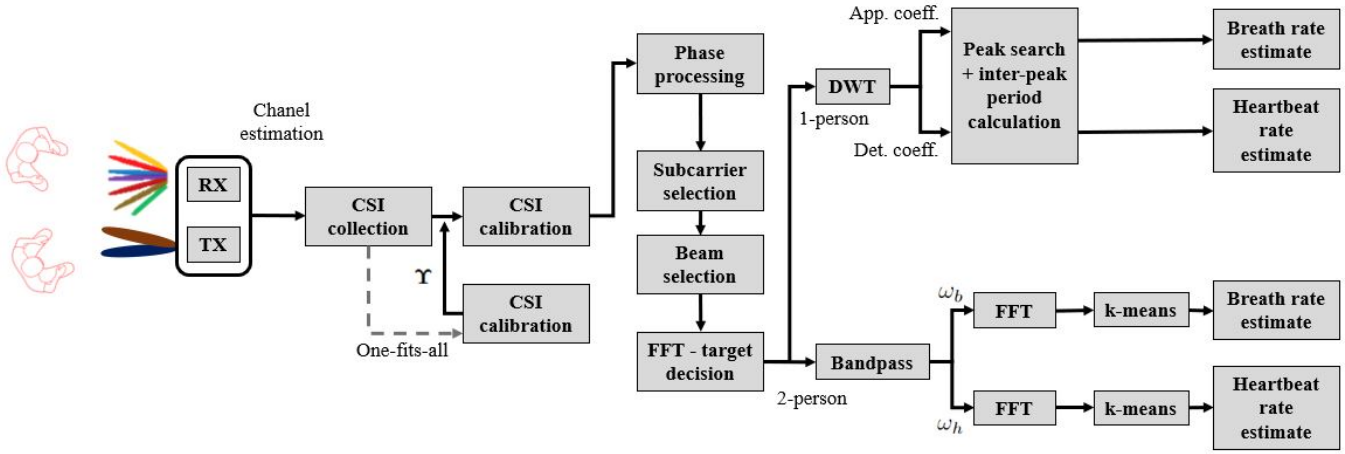

Fig. 5: Data processing pipeline for vital sign estimation.

to measure its displacement.

B. Testing Scenario 1 (TS_1)

The first testing scenario studies the raw capability of the multibeam OFDM communication system for detecting vital signs. In order to do so, the monostatic multibeam configuration in Fig. 3 is adopted. We place an absorbing foam between Tx and Rx to limit the unwanted cross-talk between each other. We place a human target in front of the Tx/Rx module and we vary the distance between human and device from 1 and up to 2 m to study the effect of distance in the estimation results. The human is static, sitting on a chair, and considered to be in the far field region of the transmitted 26 GHz beams. An schematic of TS_1 is depicted in Fig. 4.

C. Testing Scenario 2 (TS_2)

We design this measurement scenario to study the influence of the incident angle between Tx and Rx in the performance of the proposed pipeline for vital sign estimation. Thanks to the multiple beams employed in reception, we aim to study the ability of the system to obtain accurate estimates based on the spatial diversity provided by the Butler matrix. The multistatic configuration depicted in Fig. 4 for TS_2 is adopted in this testing scenario in order to obtain different incident angles based on different locations of the Tx. The Rx module is always placed in front of the human target while the distance between the human and the Rx is varied between 1 to 2 m for each Tx location. The incident angle in Fig. 4, θ_{inc}, can be defined as

$$\theta_{inc} = \arctan\left(0.95/d\right) \tag{1}$$

thus obtaining 25.4°, 32.5° and 43.5° incident angles for distances 1, 1.5 and 2 m between target and Tx respectively. For configuration number 1 and 3, we obtain 0° and 90°. Considering a human width of W m, the Rx azimuth FoV needed to cover such width when the target is located at a distance d form the Rx can be expressed as

$$\Delta_{FoV} = 2\arctan\left(\frac{W}{2d}\right) \tag{2}$$

Where W m is the width of the human being. In both TS_1 and TS_2 the target completes 3 breath cycles during 5 s. The exact breath and heartbeat frequency rate is evaluated using the ground-truth sensor.

D. Testing Scenario 3 (TS_3)

Fig. 4 shows the configuration for testing scenario 3. This testing scenario emulates a possible use of the multibeam communication system in a JCAS framework. A downlink scenario is considered. The Tx, acting as a BS, is placed 4 m away and from a Rx emulating a UE in reception mode. Two human targets are placed inside the FoV of the Tx beams. The distance between H_1 in the Y axis with respect to the Tx is varied from 1 to 3 m, while H_2 is always placed at 2 m away from the Tx in the Y axis. The separation between targets is 1 m. For all measurements, H_1 breathes at a frequency rate lower than the one of H_2. Both rates are tried to keep constant during experimental trials. Because only one ground-truth sensor is available, simultaneous ground-truth measurement on each target is not possible. Thus, measurements are repeated with the Mobi device on each target respectively and ground-truth values are obtain as the mean rates of all measurements. This needs to be accounted for when comparing the estimation results with the ground-truth values.

IV. Methodology

In this section, a processing pipeline to achieve vital sign estimation directly from captured CSI samples with a multi-beam mmWave communication testbed is explained in detail. The proposed pipeline includes time-frequency calibration to mitigate the imperfections of the RF up/down conversion chain in the estimated CSI amplitude and phase samples. The proposed pipeline also includes two different vital signs estimation methods for single and multi-person scenarios, respectively.

A. Proposed Pipeline: Overview

The proposed data processing pipeline for vital sign estimation is depicted in Fig. 5. Based on the measured scenario,

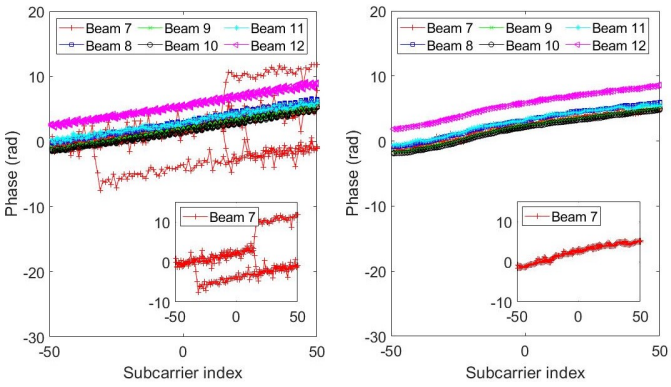

(a) Raw phase. (b) Calibrated phase.

Fig. 6: (a) Raw CSI phase data for Tx#9 and Rx beams covering the human being over 5 transmitted symbols across subcarriers. (b) CSI phase data after calibration method is applied.

the channel transfer function (CTF) is estimated in the uplink and is denoted, for a given symbol, as $\boldsymbol{H} \in \mathbb{C}^{N_R \times N_T}$:

$$\boldsymbol{H}(f, t_s) = \begin{bmatrix} h_{1,1}(f,t_s) & . & . & . & h_{1,N_T}(f,t_s) \\ . & & . & & . \\ . & & . & & . \\ . & & & . & . \\ h_{N_R,1}(f,t_s) & . & . & . & h_{N_R,N_T}(f,t_s) \end{bmatrix} \quad (3)$$

where h_{n_r,n_t} at each sampling frequency f and symbol t_s is the element of matrix $\boldsymbol{H}(f)$. N_R and N_T are the total numbers of the receive and the transmit beams, respectively. $n_r = 1, ..., 16$ and $n_t = 1, 2$ are the indices of Rx and Tx beams. For a total number of transmitted symbols, N_s, and subcarriers, N_f, the total captured channel matrix is denoted as $\boldsymbol{H} \in \mathbb{C}^{N_s \times N_f \times N_R \times N_T}$.

When the transmitted wireless signal is reflected in the chest of a human with a certain breathing and heartbeat frequency, f_b and f_h respectively, the phase of the reflected signal is also periodic with the same breathing and heartbeat frequencies [18] [31]. Let us consider the far field scenario in which a transmitted signal for a given symbol on subcarrier n_f, and for a given transmit and received pair link, is reflected from the human chest as a plane wave. Then, its phase can be written as [18] [31]:

$$\angle \boldsymbol{H}_{nr,nt}(f_{n_f}, t_s) = 2\pi \frac{d(t)}{\lambda_{n_f}} \quad (4)$$

where $d(t) = D + \alpha_b \cos(2\pi f_b t) + \alpha_h \cos(2\pi f_h t)$ is the propagation distance of the reflected signal influenced by the periodic rise and fall of the human chest. D is the constant mean distance of the reflection path, α_b and α_h are the corresponding amplitudes of the periodic signal from chest movements due to breath and heartbeat activities. λ_{n_f} is the wavelength of subcarrier n_f. Eq. 4 shows that the measured phase should increase as the subcarrier frequency increases. The received time domain phase information is clearly modulated by the breathing and heartbeat of the human

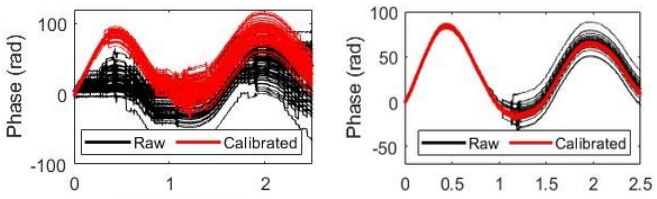

(a) (b)

Fig. 7: Phase progression of 100 subcarriers over 2.5 s capture time for Tx#9 and (a) Rx beam 8 and (b) Rx beam 9 of a human mimicking his/her breathing cycle with a metallic board.

body, and contains the necessary information for vital signs estimation, making its calibration, denoising and processing a crucial step to obtain relevant estimation rates.

After data calibration and processing, power analysis is performed on the measured channel with the objective to select the proper beams that carry information on the vital signs of the human being, while filtering out those beams that do not contain information on vital sign activity from the human being. Subcarrier selection is then performed to pick phase information on subcarriers with larger time domain variance and increase the performance of the estimation. In single-person scenario we propose Discrete Wavelet Transform (DWT) to bring the calibrated and processed data to the frequency bands of interest related to breath and heartbeat frequency rates. In this research work, DWT is proposed for frequency domain analysis because contrary to FFT analysis, DWT achieves time-frequency representation of data, providing optimal resolution both in time and frequency domains and multi-scale analysis of the transformed data. After DWT and peak search, the estimated breath and heartbeat frequency rate is obtained by taking the average of all the inter-peak interval periods from the low and high-frequency reconstructed signals, respectively. In multi-person scenario the inter-peak interval calculation after DWT on the processed phase data cannot be used to compute more than one period rate. Moreover, as breath and/or heartbeat rates are not known, we cannot use DWT to decompose the signal into the frequency bands related to the targets' vital signs activity. A solution could be to apply FFT on the decomposed signal after DWT to obtain the frequency domain behavior of the phase data.

Nevertheless, we found that the iterative decomposing steps in DWT damaged too much the "already-weak" phase periodic signal, hence failing to capture the different frequency tones of different human targets. Therefore, the pipeline employs band-pass filters to separate breath and heartbeat frequency rates in their specific bands in multi-person scenarios. This method is employed in [21]. Frequency domain analysis and peak search on Fast Fourier Transform (FFT) is then performed to estimate the number of persons in the measured scenario. The proposed pipeline novelly uses this result as the input number of clusters in the k-means algorithm to detect multiple frequency tones in both breath and heartbeat bands.

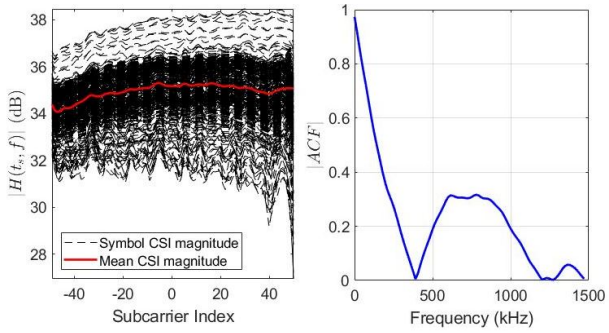

(a) TS$_1$: Monostatic radar link.

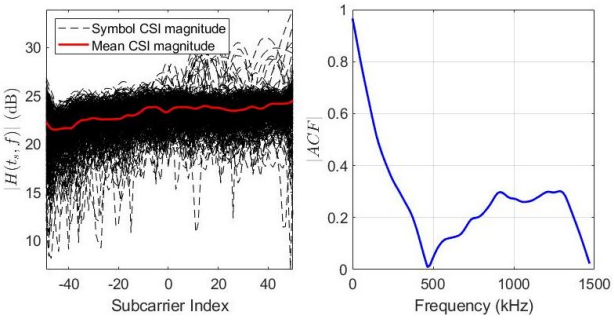

(b) TS$_3$: Communication LoS link.

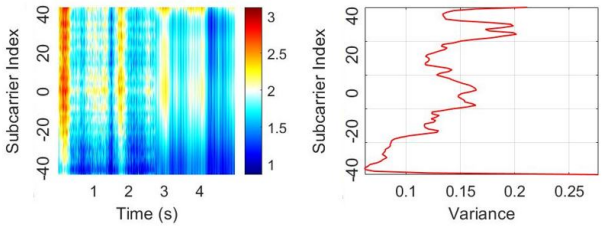

(c) TS$_1$: Monostatic radar link.

Fig. 8: (a)(b) Channel frequency response over transmitted symbols across subcarriers for central Tx beam and Rx beam 9 (left) and channel ACF (right). (c) CSI magnitude surface plot for central Tx beam and Rx beam 9 (left) and corresponding time-domain variance (right).

B. Data Calibration

During channel estimation, because of the imperfect synchronization between the transmitter and the receiver, the measured raw CSI suffers from various frequency-dependent phase errors [32]. The estimated CSI phases will suffer from the sampling frequency offset (SFO) and symbol timing offset (STO) [33]. The implementation of OFDM is susceptible to the effect of in-phase and quadrature-phase (IQ) imbalance in the analog processing. This effect can cause nonlinear phase distortion on CSI estimation. Moreover, random initial phase generated by the local oscillator and the consequent imperfect compensation of the phase-locked loop, may introduce carrier phase offsets (CPO) on the received phases [34]. In [32], a method to compensate the introduced errors in the phase measurements is presented. We adopt this method in this research. The estimated CSI at a given symbol and subcarrier

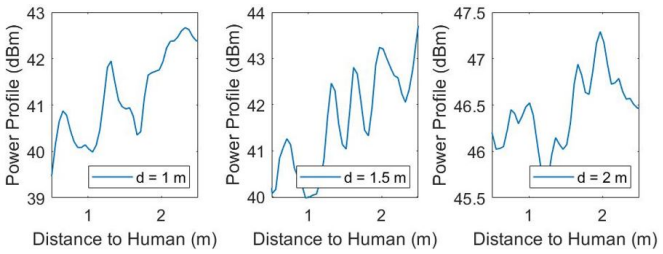

Fig. 9: Mean PDP of pair links Tx#8 - Rx#8 and Tx#9 - Rx#8.

in the presence of the aforementioned errors can be expressed as,

$$\hat{H}_{n_r,n_t} = H_{n_r,n_t} \exp\left(-j\left(\zeta_{SFO} + \zeta_{STO} + \zeta_{IQ} + \eta_{CPO}\right)\right) \tag{5}$$

where ζ_{SFO}, ζ_{STO} and ζ_{IQ} are the phase shift caused by SFO, STO, and IQ imbalance, respectively. The SFO phase shift is proportional to the subcarrier index and the ζ_{IQ} for a given subcarrier k is given by,

$$\zeta_{IQ} = \arctan\left(\epsilon_g \frac{\sin\left(n_f \xi_t + \epsilon_p\right)}{\cos\left(n_f \xi_t\right)}\right) \tag{6}$$

where ϵ_g, ϵ_p represent the gain and phase mismatch, and ξ_t is the unknown time offset, respectively. Finally, η_{CPO} can be considered as a random constant after the initiation of the transmitter. The aforementioned phase shits errors are calibrated by the following nonlinear regression:

$$\arg\min_{\boldsymbol{\Upsilon}} \sum_{n_f} \left(\Delta\Theta_{n_f} - \zeta_{IQ}^{(n_f)} - n_f \zeta_{SFO/STO} - \eta_{CPO}\right)^2 \tag{7}$$

where $\Delta\Theta_{n_k}$ is the measured residual phase at subcarrier n_k, and $\boldsymbol{\Upsilon} = [\epsilon_g, \epsilon_p, \xi_t, \zeta_{SFO/STO}, \eta_{CPO}]$. Such problem can be solved using the Levenberg-Marquardt algorithm [32]. Once the phase errors are estimated, the calibrated channel is obtained by compensating the errors in eq. 5. Note that for a given measurement setting, these parameters only need to be estimated once, and can be used for future CSI calibration directly without the redundant processing, namely one-fits-all calibration [19]. In addition to the depicted method, we apply MATLAB's *rloess* smooth filter on the calibrated data to limit the fast phase variations [35]. To test the performance of the calibration method, the Tx and Rx are collocated imitating a monostatic radar. A person holding a metallic board at chest height imitating the rise and fall of the chest during breathing cycles over 5 s is placed at 1 m of the Tx/Rx. During the captured 5 s, the human holding the metallic board performed 4 full cycles. We use the two centrals beams in transmission and the 16 beams in reception. We denote transmission beam indices as Tx#b_i and reception beam indices as Rx#b_i. Where $b_i \in [1, ..., 16]$.

In Fig. 6 raw phase is compared to calibrated phase for beams covering the human being. In general, the aforementioned frequency domain errors are not seen for all transmitted errors, but they tend to appear over sporadic symbols over certain beams. In Fig. 6a the is seen that beam Rx#7 presents

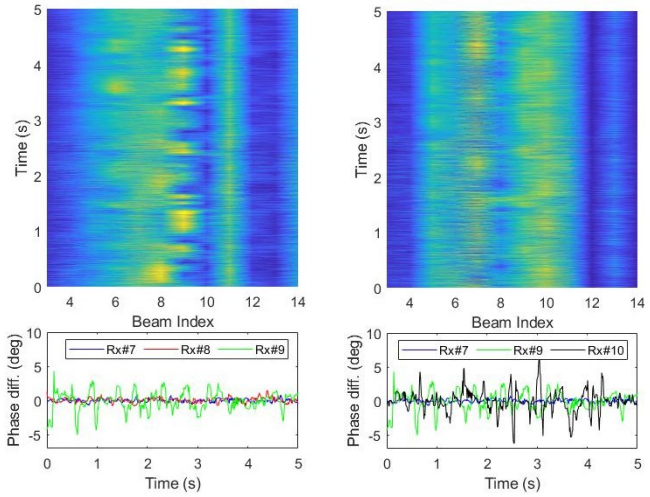

(a) Tx#8. (b) Tx#9.

Fig. 10: Calibrated CSI amplitude data across Rx beams.

variations over the used subcarriers during several of the transmitted symbols while the rest of the beams are linear with respect to subcarrier index, in line with the expected behavior of the CSI phase with respect to subcarrier index (eq. 4). In Fig. 6b it can be seen how the implemented method corrects phase errors across frequency domain to a great extent. In Fig. 7, the phase progression over the 2.5 s plotted of captured data time is recovered with the implemented method, which validates the effectiveness of the proposed phase calibration method.

After phase calibration, we further perform data processing to clean and remove the dc and high frequency noises as they have a negative impact on vital sign estimation. The dc component of the signal firstly affects subcarrier selection and further damages estimation based on peak search in the frequency domain, as it appears as a large peak at $f = 0$ Hz. High frequency noises, on the other hand, camouflage the actual frequency tones related to vital sign activity. For this, bc the dc component is not suspected to vary a lot during the length of the signal, a Hampel filter with a large sliding window of 2000 samples and a small threshold of 0.01σ is used to capture the basic trend of the original data, where σ is the standard deviation of the time domain phase samples. The detendred dc-removed phase difference data is then obtained by subtracting the basic trend from the original data. To remove high frequency noises a Hampel filter with a smaller window size is necessary, so that the fast phase variations can be filtered out. Hence we use a window size of 50 samples and a threshold of 0.01σ is employed. Because of the small phase variation due to vital signs activity, we found that a small threshold value is preferred, with 0.01σ being a value leading to a proper removal of dc and high frequency noises. Finally, downsampling is performed to lower the original high sampling frequency.

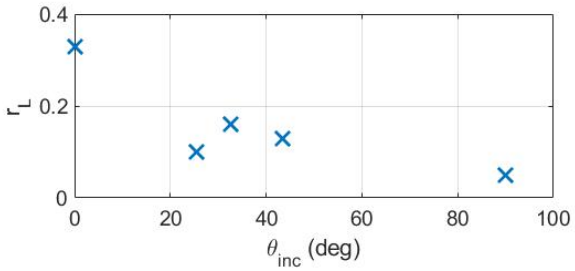

Fig. 11: Impact of incident angle on reflected power.

C. Power Analysis

Each individual receiving beam obtains information from very specific AoAs due to their narrow beamwidth. Because of the large FoV that we can cover in receiving mode with the use of the 16 orthogonal beams from the Butler matrix, it is important to make sure that the beams that actually carry information of the vital signs of the human being are used, while those who do not, are filtered out. We mainly check the time domain magnitude variations of the measured CSI samples across beams. Therefore this step is performed after subcarrier selection. Because of the sensitivity of the different subcarriers to the reflections from the human being alongside their behavior due to multipath and shadowing effects, it is important to first select those subcarriers who do not experience deep fade in the channel frequency response, so that the CSI samples from individual beams contain information related to reflections off the human being. To obtain information of the reflected power in the human body in the delay (τ) domain, we obtain the power delay profile (PDP) for a given Tx-Rx beam pair link and symbol from the CTF as [26],

$$\text{PDP}_{n_t,n_r}(:,t_s) = |\text{IFFT}\{\text{Hann}\{h_{n_t,n_r}(:,t_s)\}\}|^2 \quad (8)$$

where a Hanning window is multiplied with the CTF to suppress side-lobes. We analyse the reflection loss on the human target to study the power loss at 26 GHz of human beings. To do so, the effect of the distance-dependant path loss needs to me removed. From RF link budget theory in free-space, for a given transmission power P_T, equal transmit and receive antenna gains $G_T = G_R = G$ and received power P_R, the total loss $L = P_T + G_T + G_R - P_R$ is

$$L = L_P(d_T) + L_P(d_R) + L_R \quad (9)$$

where L_R is the reflection loss, and d_T and d_R are the distances of the object from the Tx and Rx respectively. L_P is the path loss in free-space.

We define the power reflection coefficient, r_L, as a metric to measure the reflection loss that transmitted signals experience when reflecting off the human body. We define r_L as the direct relation between the reflected P_o and incident P_i power values on the target:

$$r_L = \frac{P_o}{P_i} \quad (10)$$

P_i is defined as the summation of the transmit power, the

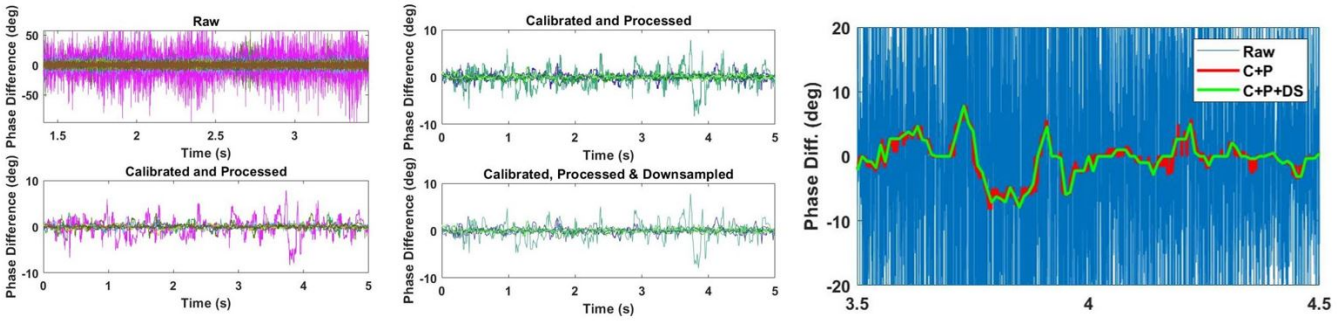

Fig. 12: Tx#9-Rx#9 phase processing on 100 subcarriers. Raw phase difference data before and after calibration and Hampel filter (left). Effect of downsampling on the calibrated and processed data (center). Time domain zoom-in calibrated, processed and downsampled data (right).

Tx gain and the path loss experienced by the plane wave at the target. P_o is taken as the value in the PDP at the target distance, removing the antenna gain and the corresponding path loss. Thus, the resulting power incident and reflected power values are not distance-dependant as path loss effects have been removed.

D. Vital Sign Estimation

As already mentioned in Section IV-A, two processing methods are implemented in this research work to analyse the capabilities of vital signs estimation of the mmWave multi-beam system. Once the time domain phase difference signal is converted to frequency domain via FFT, we use experimental results to show that in the single-person scenario only one prominent peak related to a frequency tone is found, whereas in the evaluated scenario with two-persons, the frequency domain signal shows prominent peaks related to more than one frequency tone. Hence, in single-person scenario DWT is employed to improve the performance of the estimation compared to conventional FFT and peak search method. Because DWT cannot be used in multi-person scenarios for vital signs estimation, an FFT-based combined with k-means clustering algorithm method is implemented to obtain vital signs from two humans with different vital signs activity. Prior to this, a subcarrier selection strategy is investigated to further increase performance based on frequency diversity occurring in the OFDM mmWave signals.

1) Subcarrier Analysis & Selection: During the process of the presented research work it has been observed that the magnitude and phase of the CSI samples present variations across different subcarriers, meaning that subcarriers present different sensitivity to chest displacements because they have different central frequencies and thus different wavelengths. Because of this, each individual subcarrier interacts differently when reflecting off the human body. To demonstrate this effect, we take a look at the CSI measurement data obtained in TS_1 in Fig. 4 when a human is seating 1m away from the Tx/Rx collocated module. We also analyze TS_3 in Fig. 4, when a human is placed 1 m away from the Tx in a LoS communication link.

In Fig. 8a-8b the frequency response of the channel is plotted for all transmitted symbols during the 5s capture time across subcarriers, alongside the average channel response of all transmitted symbols, for central Tx and Rx beam 9. The monostatic radar and LoS communication link are used for this analysis. The general trend illustrates a frequency flat channel response over all the bandwidth. Because of the LoS nature of the measurement scenario combined with the narrow beamwidth of the Tx and Rx beams, this behavior is expected. The transmitted signal reflects off the human chest and arrives back at the Rx without encountering possible scatterers in its path. The Rx beams receive information from AoA close to their maximum while attenuating possible multipath components arriving at different AoAs, hence the all contributions picked up by the Rx beam come directly from the human chest. Nevertheless, for some specific symbols the channel presents a frequency-selective behavior, with deep fades reaching up to 30 dB attenuation and peaks reaching up to 10 dB gain with respect to the mean value. It is noticed that the mentioned peaks mainly occur in the higher frequency components of the bandwidth. In the right figures of Fig. 8a-8b the correlation function (ACF) of the channel is plotted. In both cases we see that the 50% coherence bandwidth is 135 kHz and 150 kHz for the radar and communication configuration respectively, which is much lesser than the 15 kHz bandwidth employed by the individual subcarriers. The 90% coherence bandwidth is at around 15 kHz for both configurations, hence further validating the flat fading behavior of the channel in both tested configurations.

The CSI magnitude pattern is plotted alongside the time variance per subcarrier in Fig. 8c. It is well observed that subcarriers with larger variances are more sensitive to breathing cycles than others. Subcarriers with higher frequency and those in the vicinity of the central frequency, $n_f = [-10...10, 30...40]$, present larger variance compared to those in the lower end of the bandwidth. Moreover, in the surface plot in Fig. 8c it is also noticeable that 4 breathing cycles occur during the 5 s of captured data, corresponding to the rise and fall of the chest.

The frequency behavior of the channel can be better ex-

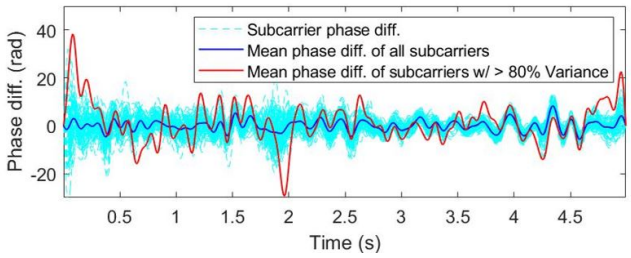

Fig. 13: Effect of subcarrier selection on phase difference data for pair link Tx#9-Rx#8.

plained using physics mechanisms. Contrary to specular reflection where the incident signal is reflected into a single outgoing direction, diffuse reflection occurs when a flat wave is scattered into multiple (random) directions due to interaction with a rough surface [36]. The condition of rough surface is described in [36] to be:

$$\Delta h > \frac{\lambda}{8 \cos \theta_{inc}} \tag{11}$$

where Δh is the rough height and θ_{inc} is the incident angle. At 26 GHz and $\theta_{inc} = 0°$ the condition is that $\Delta h > 1.44$ mm. In [37], the roughness of the human body is measured for slim, muscular and obese body type. It is found that the body roughness at the chest oscillates from 15.2 mm to 12.8 mm, respectively. Thus, the reflection of 26 GHz signals occurring at the human chest can be considered as a diffuse reflection, meaning that the incident signal will be scattered into different random directions. These reflections with random phase give birth to destructive and constructive interference at the Rx, which translates into the fades and peaks that appear in the channel frequency response for different transmitted symbols. It is therefore necessary to filter out subcarriers with low sensitivity and keep those with larger variance values to make sure estimation is performed on subcarriers carrying useful information on chest displacement due to vital signs activity. For this, a simple threshold detection method is used, where the value of such threshold is based on the experimental values obtained during the measurement campaign.

2) Single-person: The proposed vital sign single-person estimation method uses DWT to recursively decompose the phase difference data into an approximation coefficients vector with a low-pass filter and a detail coefficients vector with a high-pass filter. The approximation coefficient vector represents the low-frequency information of the input signal, while the detail coefficient vector describes the high frequency detailed information [15]. In wavelet decomposition theory, after L steps, the DWT obtains the approximation coefficient a^L and the sequence of detailed coefficients $\beta^1 ... \beta^L$ [38]. Moreover, the sampling rate is halved after each step of the decomposition process. Once the last level approximation and detailed coefficients are obtained, a peak search followed by a peak-to-peak time interval is performed in the obtained time domain decomposed signal for all the selected subcarriers. Let P_S be the number of selected subcarriers, then a set

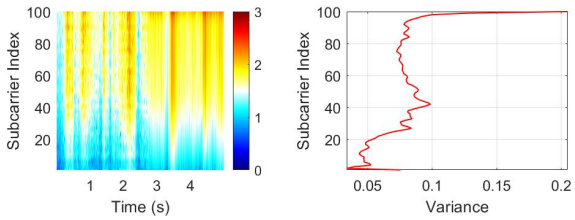

(a) TX#8-Rx#8.

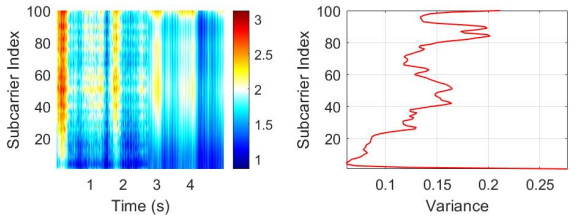

(b) TX#9-Rx#8.

Fig. 14: Variance across time and subcarrier index for central beam pair links in TS_2.

of peak-to-peak intervals from all P_S subcarriers can be expressed as $L = [l_1, ..., l_{P_S}]$, where l_i is the mean value of the vector containing the N peak-to-peak intervals obtained from the i^{th} subcarrier, where $i \in 1...P_s$. Because even if all selected subcarriers are above the measurement-based variance threshold, some of them may be more prominent than others. Therefore, we compute a weighted mean of L taking into account the variance of each subcarrier. The final estimation value is obtained as,

$$E = \sum_{i=1}^{P_S} \frac{v_i \cdot l_i}{\sum_{i=1}^{P_S} v_i} \tag{12}$$

where v_i is the variance of the i^{th} subcarrier.

A FFT-based peak search method widely used in the literature (see section II) is implemented for comparison purposes on the proposed DWT method. After prominent subcarriers carrying larger phase variations across the time samples are selected, the processed phase difference data is input to a finite impulse response (FIR) bandpass filter with a passband such of the typical frequency range of breathing and heartbeat rates. For the breathing rate (BR) we select a frequency range of 0.08 to 1 Hz (4.5 to 60 bpm). The heartbeat frequency range is selected to be 1 to 2 Hz (60 to 120 bpm), following typical and abnormal breathing and heartbeat rates [39]. Afterwards, FFT is performed in the time domain phase difference data. Let us denote ω_b as the selected frequency range for BR and ω_h the corresponding frequency range for HR, and with the time domain phase difference data denoted as $\phi(t)$ the BR and HR estimates are then computed as:

$$\hat{f}_b = \arg\max_{f \in \omega_b} |\text{FFT}(\phi(t))| \tag{13}$$

$$\hat{f}_h = \arg\max_{f \in \omega_h} |\text{FFT}(\phi(t))| \tag{14}$$

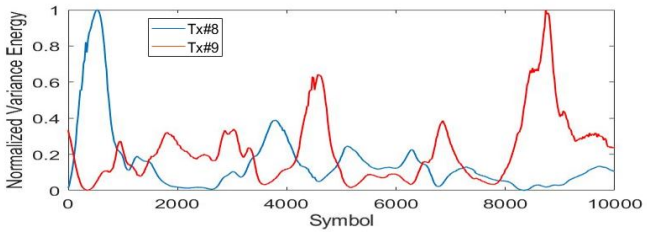

Fig. 15: Normalized variance energy at Rx#8.

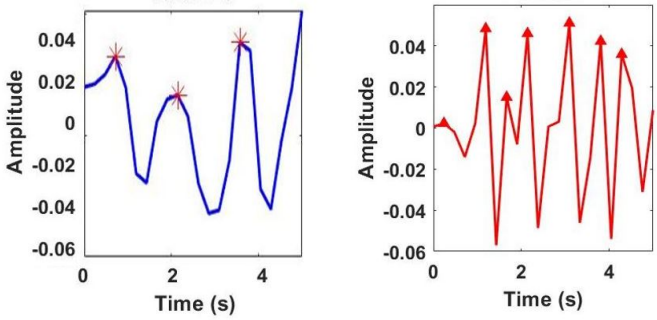

(a) (b)

Fig. 16: DWT (a) breathing and (b) heartbeat signals for Tx#9-Rx#9.

3) Multi-person: For the multi-person scenario, a FFT-based combined with k-means clustering algorithm in the frequency domain for selected subcarriers is used to obtain estimates on the breath and heartbeat rate different targets. The number of cluster targets in the measurement scenario is estimated as the number of peaks in the frequency domain signal that are above a certain power threshold. This value is served as input to the k-means algorithm. The aforementioned threshold will be later discussed based on experimental and numerical analysis. For a given selected subcarrier n_f, a peak search is performed to obtain peaks of the signal above a threshold. k-means clustering is then performed on the selected peaks. The centroid obtained from the clustering is used as the BR and/or HR estimate at that subcarrier. Given the set of centroids $C = [c_1, ..., c_{P_S}]$ from all selected subcarriers, the final estimated rate is obtained by computing the weighted mean of C using subcarrier variance as the weighting coefficients.

V. Performance Evaluation

In this section, we evaluate the performance of the proposed contact-free vital signs estimation pipeline using the mMWave multibeam testbed presented in Section III-A. The measurement setting and testing area have been introduced in Section III. The measurement campaign has been based on the three different testing scenarios introduced in Sections III-B to III-D. We use these experiments to evaluate the performance of the proposed processing pipeline under single and multi-person scenarios. The performance of the estimation is evaluated by comparing the estimates to ground-truth values.

A. Amplitude & Reflection Loss Analysis

To demonstrate the importance of amplitude analysis in beam selection and the consequential vital sign estimation, we show in Fig. 10 the amplitude of the CSI samples over time and across Rx beams for the two Tx beams in TS_1. The top figures of Fig. 10a-10b correspond to the amplitude variations over time, while the bottom figures show the extracted and processed phase difference data of beams with larger CSI amplitude. Firstly, it seen in both figures how the amplitude data has variations over time because multipath components arriving from different directions cause destructive interference at specific time domain sampling times. Rx beams 9 and 10 posses larger amplitudes when transmitting with Tx beams 8 and 9, respectively. In the bottom phase difference plots we observe how the aforementioned Rx beams posses larger phase variations related to vital sign activity than others with lower amplitude levels. Hence proving that beam selection is needed for a better estimation of vital signs. In Sec. V-B it will be further addressed the estimation performance over Rx beams.

The mean power delay profiles of the two transmitting and reception beams pairs are shown for 1, 1.5 and 2 m distance between Tx and human target in Fig. 9. The two central beams used in transmission with 7° beamwidth point towards the chest of the human being. In Fig. 9 it is observable prominent peaks at the distances where the human target is placed. When the human is placed at 1 m away from the Tx/Rx module, a prominent peak is observed at the equivalent delay distance of 1.3 m, while when the human is placed at 1.5 m and 2 m, we observe prominent peaks coming from distances 1.7 m and 2.1 m respectively. Comparing the delay indices from the prominent peaks with and without human reflections, it is observable a change of 0.3 dB in both 1 m and 2 m distances scenarios, and a 0.4 dB change in the 1.5 m scenario.

Following eq. 2, and based on Fig. 2, the r_L is computed averaging power values from the PDPs obtained at Rx beams 5 to 12, 6 to 11 and 7 to 10, to ensure reflections coming from the human target. Fig. 11 shows the resulting reflection coefficient values for the aforementioned values at 26 GHz, for the linearly polarized beam impinging parallelly with respect to the incident plane. Although not being a thorough characterization, some general trends can be observed. Around 35% of the incident power is reflected off the human chest at normal incident angle and the reflection loss coefficient decreases as the incident angle increases. Based on the measurement setting (see Section III-B), this behavior is expected as when the incident angle is increased we expect less reflections being captured at the Rx beams. These results are in accordance with the values obtained *Wu et al.* [40] based on simulated theoretical models.

B. Single-person Vital Signs Estimation

Using the different configurations of the testing scenarios, we now study the capability of the proposed pipeline for vital sign estimation in a single-person scenario. An example of CSI phase data calibration and processing is depicted in Fig.

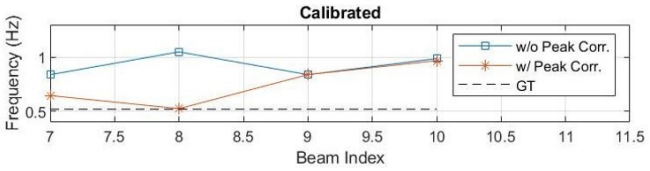

Fig. 17: False peak detection and removal example using subcarrier selection.

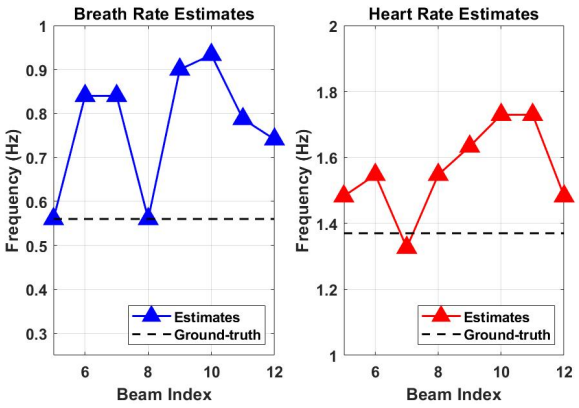

Fig. 18: Breath rate estimates (left) and heartbeat rate estimates (right) for monostatic radar-like configuration with the human placed 3 m from the Tx for Tx#9-Rx#5:12 beams.

12 for pair links Tx#9-Rx#1:16. It is observed how the raw CSI phase difference data contains very fast variations. After phase calibration to remove hardware nonlinearities, Hampel filter is used to obtain the trend of the signal, which is then removed from the original signal, thus eliminating DC components on the phase data that can affect the frequency domain transformation for vital sign estimation. Finally, downsampling is performed to acquire a more manageable data size. In this work a donwsampling factor (DS) of 20 is implemented to bring the original 2000 Hz sampling frequency and 10000 time samples down to 100 Hz and 500, sampling frequency and time samples respectively.

Subcarrier selection is an important step in vital sign estimation. In Fig. 13, individual subcarrier phase differences are plotted compared to the mean phase difference across all subcarriers and the mean phase difference of subcarriers with $>$ 80% of the maximum variance across time domain. Fig. 14a shows surface CSI amplitude samples versus time and Fig. 14b depicts time domain variance versus subcarrier index, for the two Tx beams received at Rx#8. The impact of chest displacement due to breathing activity is noticeable specially in Fig. 15, where the normalized variance energy per beam is defined as

$$NVE = \frac{1}{N_f N_s} \sum_{n_f=1}^{N_f} \sum_{t_s=1}^{N_s} \left| v_{n_f}(t_s) \right| \tag{15}$$

where $v_{n_f}(n)$ is the variance value at subcarrier n_f and symbol t_s, obtained from the variance matrix $\boldsymbol{V} = \left[V_1, ..., V_{N_f}\right]$ with $V_{n_f} = \left[v_1(1), ..., v_{N_f}(N_s)\right]^T$. Variance values per subcarriers are spliced in time sample windows at which the cumulative variance energy is obtained. The results show three time intervals where variance energy is concentrated related to the three breathing cycles performed by the human being. Once the data is processed, we employ DWT with L = 4 steps and Daubechies wavelet filters of level 4. As mentioned in Section IV, we perform search peak on the approximation and detailed coefficients to obtain breath and heartbeat rates, respectively. In Fig. 16 it is shown the extracted DWT breathing and heartbeat signals for Rx beam 9 when transmitting with beam 8. The time positions of the peaks are subtracted from their respective following peak, to obtain the period P. The rate is then computed in Hz as $1/P$ or $60/P$ in bpm. The ground-truth rates are 0.56 Hz and 1.37 Hz for breath and heartbeat activities respectively. The prior knowledge of typical breathing and heartbeat values from human beings is leveraged to remove false detected peaks on DWT. Such peaks that present inter-peak interval times outside range of typical values are deleted. Estimation results shown in Fig. 17 show the importance of the false peak removal method for the breathing cycle. In all Rx beams, using the proposed method leads an enhanced estimation. The estimation on Rx beam 8 using prominent subcarriers achieves the best result as expected, as the beam is directly pointing to the human chest.

An example of DWT-based estimation results for Rx beams 5-12 is shown in Fig. 18. Rx beams 5 and 8 achieve perfect breath rate estimation compared to the ground-truth. This is expected for Rx#8 as the beam is directly pointing to the human chest. For the case of Rx#5, results show that signals reflecting in the human chest can also be picked up from different azimuth angles due to multipath richness. For heartbeat rate estimates, Rx#7 achieves 1.2 bpm absolute error. Overall, from Fig. 18 it is seen that the estimation is very poor for those Rx beams not picking up contributions from reflected signals on the human chest, but highly accurate from beams picking up reflections from the human chest; demonstrating the capability of individual Tx-Rx pair links to obtain accurate vital sign information. However, because in real life applications the ground-truth is not known, a decision must be made including all information picked up from beams inside the human's chest FoV. We propose a weighted mean method, in which the weighting coefficients are the time-domain average variance values from all selected subcarriers. The estimation is unavoidably degraded, with estimation values increasing to 7.5 bpm and 11.4 bpm for breath and heartbeat activity, respectively.

Moreover, there is a clear overestimation for different beams affecting both breath and heart rate estimates similarly. An overestimation of the frequency rate translates into an underestimation of the breathing and heartbeat periods extracted from the DWT decomposed low and high-frequency signals in the band of interest, meaning that the obtained mean inter-peak interval is actually smaller than the ground-truth one. The

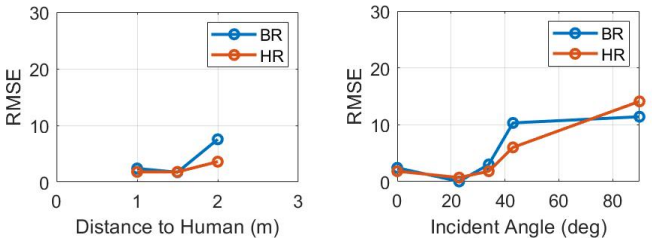

(a) (b)

Fig. 19: Estimation RMSE values for Tx#9-Rx#8 pair link.

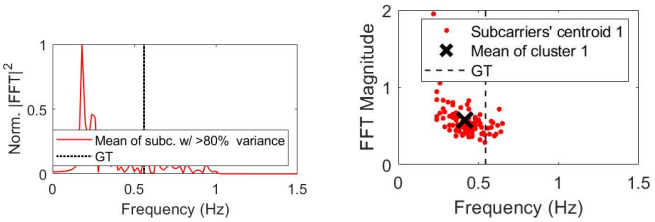

(a) (b)

Fig. 20: Tx#9-Rx#8: (a) FFT-based single person estimate. (b) FFT with k-means clustering single person estimate.

DWT decomposition on beams not carrying information on the vital signs of the person generally produces false peaks, with small amplitude, that do not correspond to vital sign activity but are still considered after the correction mechanism because they still are inside the bounds of the vital sign periods used in the correction step. Another reason is that in the 5s of capture time there are around 3 and 7 full breath and heartbeat cycles, respectively. Meaning that the average inter-peak interval has very small number of samples, amplifying the importance of the DWT method to precisely extract the correct frequency tones.

RMSE values with respect to distance and incident angles are plotted in Fig. 19 for monostatic radar-like configuration 1, 2 and 3 in TS_2. These values are obtained by the DWT method for each Rx beam and selecting the beam with a smaller RMSE value. Hence, the results in Fig. 19 represent the case in which the best performing Rx beams are selected as the final estimation result. Although not having a very representative data set, we observe a general trend that the estimation error increases as both distance and incident angle increase. A reason for this is that at larger distances reflected signals are more attenuated, and at large incident angles reflected signals modulated by the human chest may be not picked up by beams with larger gains. Also, breath rate and heartbeat rate RMSE values are kept under 5 bpm at 1 and 1.5 m and for all distances, respectively. Breath rate is kept under 5 bpm for incident angles below 40 degrees, while heartbeat rate achieves this for angles below up to 40 degrees.

The FFT-based method depicted in section IV is used to compare it to the proposed DWT-based method. Fig. 20a shows the frequency domain mean power signal of subcarriers with $>$80% of the maximum variance value of the Tx#9-Rx#8 pair link for the monostatic radar-like configuration with the human placed at 1 m from the Tx. Typical FFT-based methods for vital sign estimation found in the literature (see section II), rely on selecting the maximum peak from such signal. Using this method in Fig. 20a, we obtain an absolute error of more than 20 bpm compared to the ground-truth. In Fig. 20b the selected individual subcarrier's centroids are depicted in red dots. The mean weighted average of these points is show as the black cross, taking the variance of each subcarrier as the weighting factors. We thus observe an absolute error of 0.1435 Hz (8.61 bpm) compared to the ground-truth, which is $>$7 bpm worse than the one obtained with the proposed DWT-method for the same Tx-Rx pair link.

C. Multi-person Vital Signs Estimation

The two person measurements obtained from TS_3 are analysed in this subsection. As mentioned, the two measured targets breathe at different rates. The ground-truth breath rates values for these targets are 0.35 Hz (21 bpm) and 0.69 Hz (41.1 bpm). Firstly, let us compare the normalized frequency power illustrated in figures 20a and 21. Compared to the one person scenario, two prominent peaks are seen in the two person scenario. We use this experimental result, which we have observed through our research work to determine the number of targets input to the k-means algorithm for estimating rates. Estimation results for the breathing rate are depicted in Fig. 22. Based on the geometry of TS_3 and the Butler matrix pattern some insights can be drawn. For instance, taking a look at Fig. 22a and Fig. 22b where transmission is performed with Tx#9, it is observable that estimation on H_1 is poorer than the one for H_2. This is because the beam used in transmission is mainly pointing to H_2, hence reflections will be larger modulated by its frequency. Nevertheless, the Tx beam is also capable of reaching H_1, modulating reflected signals with its frequency. In this case, Rx#6 and Rx#12 have 0 and 1.5 bpm error values. When transmitting with Tx#9, the error is kept under 2 bpm in all cases for both targets in Fig. 22c and Fig. 22d. The presented results for the two-person scenario reveal that individual beams have the capability of recovering information from reflected signals in an indoor environment thanks to the rich multipath environment. The estimation performance relates directly to the geometry of the scenario and the orientation of the Tx and Rx beams, which can be leveraged to also obtain vital sign estimation on targets breathing at similar rates. More experimental evaluation is needed to fully evaluate the performance of such pipeline in those circumstances. For instance, further evaluation is needed to clearly define a mapping strategy of the locations covered by the Tx-Rx pair links combining reflection loss analysis and vital sign extraction. In this context, with such strategy, a clear view on the location of the targets should be achieved, helping make a decision strategy for when Tx-Rx pair links contain information of two or more targets breathing at the same rate; which the current state of the algorithm would only

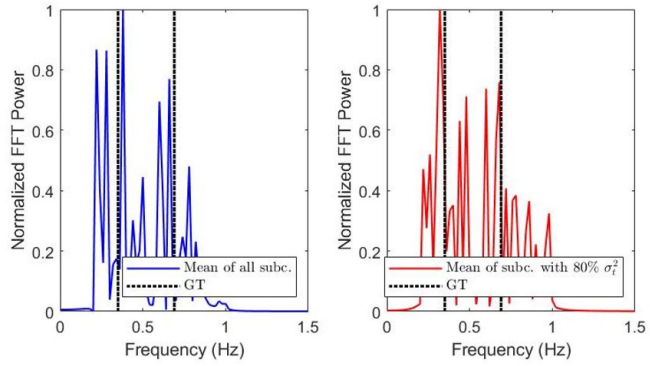

Fig. 21: FFT analysis of the two person scenario. Mean value of all subcarriers (left) and mean value of >80% variance subcarriers (right), for pair link Tx#9-Rx#12.

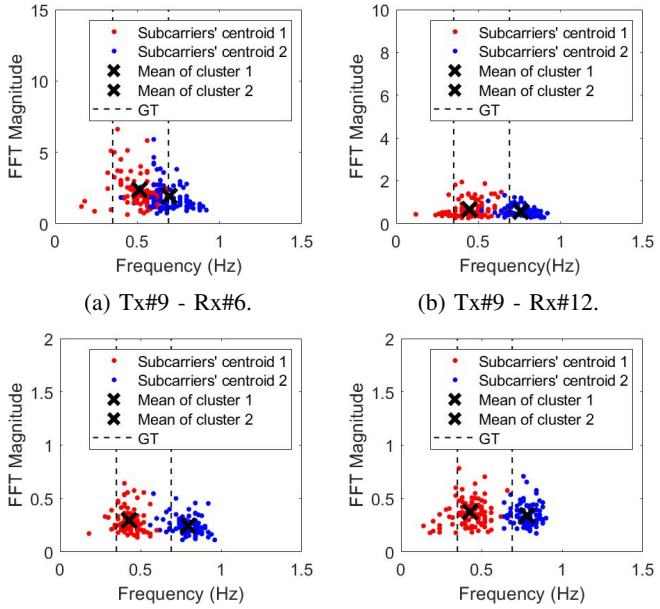

(a) Tx#9 - Rx#6. (b) Tx#9 - Rx#12.

(c) Tx#8 - Rx#6. (d) Tx#8 - Rx#12.

Fig. 22: Breath rate estimates in two person scenario.

detect as one target. In short, this small study reveals that joint communication and sensing can be possible in mmWave multibeam systems, with the possibility to dedicate specific communication beams to sensing activities.

VI. Conclusion

In this paper, the capability of a 26 GHz multibeam OFDM testbed for vital signs estimation has been studied based on a measurement campaign on single and multi-person scenarios. A post-processing pipeline algorithm is introduced, implemented and put under test to evaluate the performance of vital sign estimation, in single and multi-person indoor scenarios, which are useful for joint communication and sensing applications. The pipeline includes frequency and time domain calibration of the captured CSI samples to remove frequency-phase nonlinearities introduced by the up/downcoversion RF chain and a proposed method for a correct high frequency denoising. Two different methods are proposed based on single or multi-person scenarios. DWT is employed in single-person scenarios to obtain better estimates compared to FFT-based methods found in the literature. For multi-person scenarios, FFT and k-means clustering algorithm is employed to obtain vital sign information from different targets. The influence of frequency diversity and fading is also studied.

Reflection loss has been studied and compared to some incident angles. It is find out that reflection loss is larger at the normal incident angle with 35% of the incident power reflected. The proposed methodology in monostatic radar-like configuration further reveals that DWT can offer estimation performance below 2 bpm absolute error for individual Tx and Rx beam pair links, while using FFT-based methods the error can increase to 8 bpm. In monostatic radar-like configuration results reveal that the RMSE increases with the incident angle. In two-person scenario, the proposed vital sign estimation method, based on frequency analysis and k-means clustering, reveals that individual beams are able to pick up reflections coming from different targets while offering 3 bpm absolute error, which opens up the possibility to dedicate specific beams to sensing activities in active mmWave multibeam communication.

This paper demonstrates our preliminary investigation on the raw capability of mmWave OFDM multibeam systems to simultaneously perform active communication and sensing in future generations of mobile communications. It deserves further and extensive exploration. Future lines of work should include a more extensive measurement campaign covering more Tx/Rx locations to have a better insight on the influence of distance and incident angle in both reflection and vital signs estimation. For this, a more controlled scenario like a anechoic chamber should be used. Using a controlled scenario should also be helpful to make sure multipath components are well accounted for. Such extensive campaign should also make it possible to better evaluate the proposed pipeline in real-world indoor scenarios for more than two targets, and simultaneously evaluate the capability of the system for joint active and sensing activities. Based on the spatial diversity of the multibeam system, mapping targets in space based on their vital signs could also be an interesting application in a future line of work.

Acknowledgment

The author would like to thank the ESAT department at the KU Leuven for the use of the 26 GHz multibeam OFDM testbed to perform the measurement campaign. More specifically, members Rizqi Hersyandika and Robbert Beerten for their guidance in the use of the system and the their help in the measurement campaign. Also, dr. Ying Wang for the use and help with the vital signs ground-truth device. Finally, the author would like to express his gratitude to dr. Yang Miao for her guidance during all the research process.

REFERENCES

[1] A. Bourdoux, A. N. Barreto, B. van Liempd, C. de Lima, D. Dardari, D. Belot, E.-S. Lohan, G. Seco-Granados, H. Sarieddeen, H. Wymeersch, J. Suutala, J. Saloranta, M. Guillaud, M. Isomursu, M. Valkama, M. R. K. Aziz, R. Berkvens, T. Sanguanpuak, T. Svensson, and Y. Miao, "6g white paper on localization and sensing," 2020. [Online]. Available: https://arxiv.org/abs/2006.01779

[2] T. Wild, V. Braun, and H. Viswanathan, "Joint design of communication and sensing for beyond 5g and 6g systems," *IEEE Access*, vol. 9, pp. 30 845–30 857, 2021.

[3] S. D. Liyanaarachchi, T. Riihonen, C. B. Barneto, and M. Valkama, "Optimized waveforms for 5g–6g communication with sensing: Theory, simulations and experiments," *IEEE Transactions on Wireless Communications*, vol. 20, no. 12, pp. 8301–8315, 2021.

[4] C. B. Barneto, S. D. Liyanaarachchi, T. Riihonen, L. Anttila, and M. Valkama, "Multibeam design for joint communication and sensing in 5g new radio networks," in *ICC 2020 - 2020 IEEE International Conference on Communications (ICC)*, 2020, pp. 1–6.

[5] H. Wymeersch, D. Shrestha, C. M. de Lima, V. Yajnanarayana, B. Richerzhagen, M. F. Keskin, K. Schindhelm, A. Ramirez, A. Wolfgang, M. F. de Guzman, K. Haneda, T. Svensson, R. Baldemair, and S. Parkvall, "Integration of communication and sensing in 6g: a joint industrial and academic perspective," 2021. [Online]. Available: https://arxiv.org/abs/2106.13023

[6] M. S. Mahmud, H. Wang, A. M. Esfar-E-Alam, and H. Fang, "A wireless health monitoring system using mobile phone accessories," *IEEE Internet of Things Journal*, vol. 4, no. 6, pp. 2009–2018, 2017.

[7] M. C. Caccami, M. Y. S. Mulla, C. Occhiuzzi, C. Di Natale, and G. Marrocco, "Design and experimentation of a batteryless on-skin rfid graphene-oxide sensor for the monitoring and discrimination of breath anomalies," *IEEE Sensors Journal*, vol. 18, no. 21, pp. 8893–8901, 2018.

[8] X. Liu, J. Yin, Y. Liu, S. Zhang, S. Guo, and K. Wang, "Vital signs monitoring with rfid: Opportunities and challenges," *IEEE Network*, vol. 33, no. 4, pp. 126–132, 2019.

[9] R. Zhao, D. Wang, Q. Zhang, H. Chen, and A. Huang, "Crh: A contactless respiration and heartbeat monitoring system with cots rfid tags," in *2018 15th Annual IEEE International Conference on Sensing, Communication, and Networking (SECON)*, 2018, pp. 1–9.

[10] F. Adib, H. Mao, Z. Kabelac, D. Katabi, and R. C. Miller, "Smart homes that monitor breathing and heart rate," in *Proceedings of the 33rd Annual ACM Conference on Human Factors in Computing Systems*. New York, NY, USA: ACM, Apr. 2015.

[11] T. Instruments, "Mmwave radar sensors." [Online]. Available: https://www.ti.com/sensors/mmwave-radar/overview.html

[12] N. Patwari, L. Brewer, Q. Tate, O. Kaltiokallio, and M. Bocca, "Breathfinding: A wireless network that monitors and locates breathing in a home," *IEEE Journal of Selected Topics in Signal Processing*, vol. 8, no. 1, pp. 30–42, 2014.

[13] H. Abdelnasser, K. Harras, and M. Youssef, "Ubibreathe: A ubiquitous non-invasive wifi-based breathing estimator," 05 2015.

[14] R. Ravichandran, E. Saba, K.-Y. Chen, M. Goel, S. Gupta, and S. N. Patel, "Wibreathe: Estimating respiration rate using wireless signals in natural settings in the home," in *Pervasive Computing and Communications (PerCom), 2015 IEEE International Conference on*. IEEE, 2015, pp. 131–139.

[15] D. Zhang, Y. Hu, Y. Chen, and B. Zeng, "Breathtrack: Tracking indoor human breath status via commodity wifi," *IEEE Internet of Things Journal*, vol. 6, no. 2, pp. 3899–3911, 2019.

[16] X. Wang, C. Yang, and S. Mao, "Phasebeat: Exploiting csi phase data for vital sign monitoring with commodity wifi devices," in *2017 IEEE 37th International Conference on Distributed Computing Systems (ICDCS)*, 2017, pp. 1230–1239.

[17] A. Eid, J. Zhu, L. Xu, J. G. D. Hester, and M. M. Tentzeris, "Holography-based target localization and health monitoring technique using uhf tags array," *IEEE Internet of Things Journal*, vol. 8, no. 19, pp. 14 719–14 730, 2021.

[18] D. Zhang, Y. Hu, and Y. Chen, "Mtrack: Tracking multiperson moving trajectories and vital signs with radio signals," *IEEE Internet of Things Journal*, vol. 8, no. 5, pp. 3904–3914, 2021.

[19] C. Li, S. De Bast, Y. Miao, E. Tanghe, S. Pollin, and W. Joseph, "Contact-free multi-target tracking using distributed massive mimo-ofdm communication system: Prototype and analysis," 2022. [Online]. Available: https://arxiv.org/abs/2208.10863

[20] M. Mercuri, I. R. Lorato, Y.-H. Liu, F. Wieringa, C. Van Hoof, and T. Torfs, "Vital-sign monitoring and spatial tracking of multiple people using a contactless radar-based sensor," *Nature Electronics*, vol. 2, no. 6, pp. 252–262, Jun. 2019.

[21] A. Ahmad, J. C. Roh, D. Wang, and A. Dubey, "Vital signs monitoring of multiple people using a fmcw millimeter-wave sensor," in *2018 IEEE Radar Conference (RadarConf18)*, 2018, pp. 1450–1455.

[22] Z. Xu, C. Shi, T. Zhang, S. Li, Y. Yuan, C.-T. M. Wu, Y. Chen, and A. Petropulu, "Simultaneous monitoring of multiple people's vital sign leveraging a single phased-mimo radar," *IEEE Journal of Electromagnetics, RF and Microwaves in Medicine and Biology*, vol. 6, no. 3, pp. 311–320, 2022.

[23] T. Sakamoto, "Noncontact measurement of human vital signs during sleep using low-power millimeter-wave ultrawideband mimo array radar," in *2019 IEEE MTT-S International Microwave Biomedical Conference (IMBioC)*, vol. 1, 2019, pp. 1–4.

[24] L. J. Dirksmeyer, A. Marnach, D. Schmiech, and A. R. Diewald, "Developing of algorithms monitoring heartbeat and respiration rate of a seated person with an fmcw radar," *Advances in Radio Science*, vol. 19, pp. 195–206, 2021. [Online]. Available: https://ars.copernicus.org/articles/19/195/2021/

[25] X. Wang, M. Laabs, D. Plettemeier, K. Kosaka, and Y. Matsunaga, "28 ghz multi-beam antenna array based on wideband high-dimension 16x16 butler matrix," in *2019 13th European Conference on Antennas and Propagation (EuCAP)*, 2019, pp. 1–4.

[26] R. Hersyandika, Q. Wang, S. Pollin, Y. Miao, and F. Tufvesson, "Measurement-based analysis of mmwave multi-point connectivity approaches in blocked scenarios," 2022.

[27] A. Colpaert, E. Vinogradov, and S. Pollin, "Fixed mmwave multi-user mimo: Performance analysis and proof-of-concept architecture," in *2020 IEEE 91st Vehicular Technology Conference (VTC2020-Spring)*, 2020, pp. 1–5.

[28] N. Instruments, "5g massive mimo testbed: From theory to reality," 2021. [Online]. Available: https://www.ni.com/en-us/innovations/white-papers/14/5g-massive-mimo-testbed–from-theory-to-reality–.html

[29] "Labview communications mimo application framework 19.5 readme." [Online]. Available: https://www.ni.com/pdf/manuals/377191e.html

[30] TMSi, "User manual: Mobi." [Online]. Available: https://info.tmsi.com/user-manual-mobi

[31] X. Wang, C. Yang, and S. Mao, "Phasebeat: Exploiting csi phase data for vital sign monitoring with commodity wifi devices," in *2017 IEEE 37th International Conference on Distributed Computing Systems (ICDCS)*, 2017, pp. 1230–1239.

[32] C. Li, S. De Bast, E. Tanghe, S. Pollin, and W. Joseph, "Toward fine-grained indoor localization based on massive mimo-ofdm system: Experiment and analysis," *IEEE Sensors Journal*, vol. 22, no. 6, pp. 5318–5328, 2022.

[33] M. Speth, S. Fechtel, G. Fock, and H. Meyr, "Optimum receiver design for wireless broad-band systems using ofdm. i," *IEEE Transactions on Communications*, vol. 47, no. 11, pp. 1668–1677, 1999.

[34] A. Tarighat, R. Bagheri, and A. Sayed, "Compensation schemes and performance analysis of iq imbalances in ofdm receivers," *IEEE Transactions on Signal Processing*, vol. 53, no. 8, pp. 3257–3268, 2005.

[35] Mathworks, "smooth." [Online]. Available: https://nl.mathworks.com/help/curvefit/smooth.html

[36] M. Gan, *Accurate and low-complexity ray tracing channel modeling*. TU Wien, 2015.

[37] S. Ritter, K. Staub, and P. Eppenberger, "Associations between relative body fat and areal body surface roughness characteristics in 3d photonic body scans—a proof of feasibility," *International Journal of Obesity*, vol. 45, pp. 1–8, 04 2021.

[38] S. Sardy, P. Tseng, and A. Bruce, "Robust wavelet denoising," *IEEE Transactions on Signal Processing*, vol. 49, no. 6, pp. 1146–1152, 2001.

[39] J. F. Murray, *The normal lung : the basis for diagnosis and treatment of pulmonary disease / John F. Murray*. Saunders Philadelphia, 1976.

[40] T. Wu, T. S. Rappaport, and C. M. Collins, "The human body and millimeter-wave wireless communication systems: Interactions and implications," in *2015 IEEE International Conference on Communications (ICC)*, 2015, pp. 2423–2429.